

# Single-Camera Focus-Based Localization of Intraocular Devices

Christos Bergeles\*, *Student Member, IEEE*, Kamran Shamaei, Jake J. Abbott, *Member, IEEE*, and Bradley J. Nelson, *Senior Member, IEEE*

**Abstract**—Future retinal therapies will be partially automated in order to increase the positioning accuracy of surgical tools. Proposed untethered microrobotic approaches that achieve this increased accuracy require localization information for their control. Since the environment of the human eye is externally observable, images can be used to localize the microrobots. In this paper, the common methods of ophthalmoscopy assuming a single stationary camera are examined and compared with respect to their imaging and localizing properties on a schematic model of the human eye. The first algorithm for wide-angle intraocular localization based on indirect ophthalmoscopy is presented, and its sensitivity with respect to uncertainties in the parameters of individual eyes is estimated. A calibration technique to account for these uncertainties is proposed, and the localization algorithm is validated with experiments in a model eye.

**Index Terms**—Eye, imaging, intraocular, localization, microrobot, ophthalmoscopy, tracking.

## I. INTRODUCTION

VITREORETINAL surgery requires accuracy and dexterity that is often beyond the limits of human surgeons. Robot-assisted solutions have been developed to improve the surgeons' ability to perform these difficult procedures [1]–[5]. Our work is motivated by the wireless magnetic intraocular microrobot proposed in [5]. This microrobot, which can also be thought of as the end-effector of a wireless micromanipulation system, will be inserted through the *pars plana* region of the sclera, wirelessly controlled down to the retina to perform the desired procedure under teleoperation or supervisory control of a surgeon, and then wirelessly controlled back to the entry point to be removed by

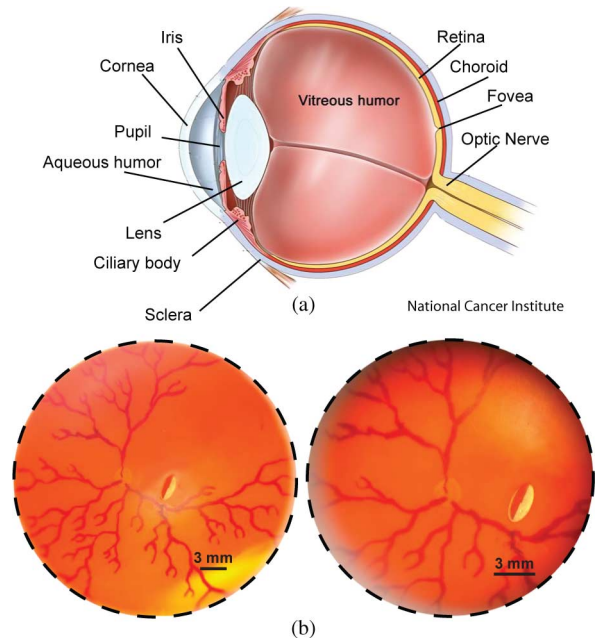


Fig. 1. (a) Anatomy of the human eye. (b) The biomedical microrobot of [5] in a model eye [9]. The left image shows the intraocular environment without the eye's optical elements, and the right image shows the effect of the model eye's optics. Images are taken with an unmodified digital camera.

a magnetic tool. This will enable less invasive and safer retinal surgery, as well as an increased level of dexterity desired by clinicians.

For precise magnetic control, knowledge of the position of the untethered device within the magnetic field is needed [6], [7]. Our primary motivation is to provide position information to an electromagnetic control system [8]. Since the interior of the human eye is externally observable, vision-based 3-D localization is possible.

Ophthalmic observation has been practiced for centuries, and clinicians have the ability to acquire high-definition and magnified images of the interior of the eye using a variety of optical tools. However, the optical elements of the eye [see Fig. 1(a)] limit the field of view, alter the formation of images [see Fig. 1(b)], and make localization challenging.

We must perform 3-D localization and imaging with a single stationary camera while allowing for focusing motions because of the limited workspace above the eye. Common techniques for the localization of objects from monocular images assume a calibrated imaging system [13]. However, in our case, calibrating the entire optical system is infeasible because of the

Manuscript received October 6, 2009; revised December 21, 2009; accepted February 7, 2010. Date of publication May 3, 2010; date of current version July 14, 2010. This work was supported by the NCCR Co-Me of the Swiss National Science Foundation. Asterisk indicates corresponding author.

\*C. Bergeles is with the Institute of Robotics and Intelligent Systems, ETH Zurich, 8092 Zurich, Switzerland (e-mail: cbergeles@ethz.ch).

K. Shamaei was with the Institute of Robotics and Intelligent Systems, ETH Zurich, 8092 Zurich, Switzerland. He is now with the School of Engineering and Applied Science, Yale University, New Haven, CT 06520 USA (e-mail: kamran.shamaei@yale.edu).

J. J. Abbott was with the Institute of Robotics and Intelligent Systems, ETH Zurich, 8092 Zurich, Switzerland. He is now with the Department of Mechanical Engineering, University of Utah, Salt Lake City, UT 84112 USA (e-mail: jake.abbott@utah.edu).

B. J. Nelson is with the Institute of Robotics and Intelligent Systems, ETH Zurich, 8092 Zurich, Switzerland (e-mail: bnelson@ethz.ch).

Color versions of one or more of the figures in this paper are available online at <http://ieeexplore.ieee.org>.

Digital Object Identifier 10.1109/TBME.2010.2044177

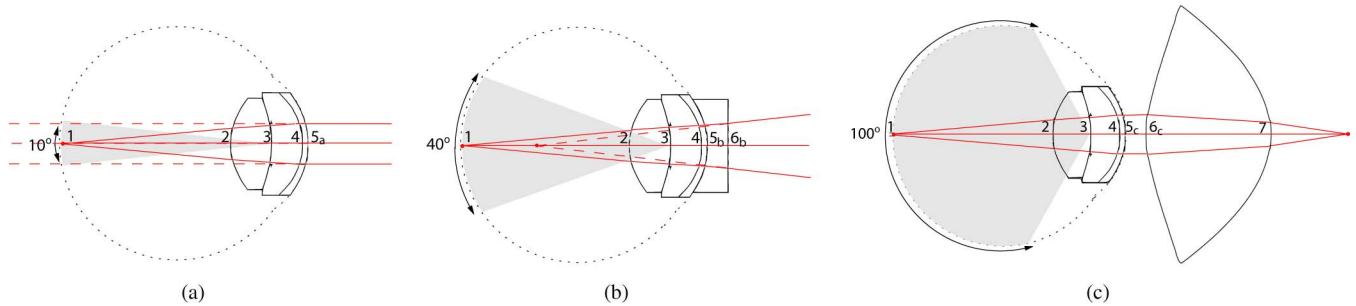


Fig. 2. (a) Direct ophthalmoscopy with Navarro's schematic eye [10]. (b) Ophthalmoscopy with Navarro's schematic eye with a vitrectomy lens [11]. (c) Indirect ophthalmoscopy with Navarro's schematic eye with a condensing lens [12].

inaccessibility of the interior of the human eye and its unique optics. Other methods for depth extraction involve using focus/defocus information [14], [15]. Focus-based methods do not require a model of the object, only knowledge of the optical system. As a result, our analysis is applicable on any type of unknown foreign bodies. For example, in [16], [17], fluorescent particles are tracked in fluids using defocus information. Additionally, focus-based methods can be used to estimate the position of surgical tools, and provide feedback to the surgeon. Depth from defocus is proposed in [18] as a method to visually servo intraocular microrobots, but the optics of the eye are not considered.

In this paper, we account for the optics of the human eye in the imaging and localization of intraocular objects with a stationary camera. In Section II, we evaluate different ophthalmoscopy methods. In Section III, we present our wide-angle intraocular localization algorithm, we investigate its sensitivity with respect to variations in human eyes, and we propose a calibration method to correct for the errors resulting from parameter uncertainties. In Section IV, we demonstrate the validity of the algorithm by experiments in a model eye. The paper concludes in Section V. Parts of this work have appeared in [19]–[21].

## II. COMPARISON OF OPHTHALMOSCOPY METHODS

Our results are based on Navarro's schematic eye [10] (i.e., an optical model based on biometric data that explains the optical properties of the human eye). Navarro's schematic eye performs well for angles up to  $70^\circ$  measured from the center of the pupil and around the optical axis. For greater angles, the biometric data of each patient should be considered individually. The pupil diameter in [10] is 3 mm. Simulations are carried out with the OSLO optical lens design software. The object's depth is measured along the optical axis. We begin by investigating the feasibility of imaging and localizing intraocular devices using existing ophthalmoscopy methods. We assume that we have sufficient illumination to acquire the images.

### A. Direct Ophthalmoscopy

Direct ophthalmoscopy involves direct observation of the human eye retina by a clinician [22]. Based on [23], the field of view is found at  $10^\circ$  [see Fig. 2(a) and Table I]. The formed image of the intraocular objects is always virtual (see Fig. 3 solid line), and capturing it requires an imaging system with a nearly

TABLE I  
OPTICAL PARAMETERS FOR THE SYSTEMS OF FIG. 2

Surface	Radius	Conic Constant	Thickness	Index
1	12.00 mm	0.00	16.32 mm	1.336
2	6.00 mm	−1.00	4.00 mm	1.420
3	−10.20 mm	−3.13	3.05 mm	1.337
4	−6.50 mm	0.00	0.55 mm	1.376
5a	−7.72 mm	−0.26	$\infty$ mm	1.000
5b	−7.72 mm	−0.26	2.00 mm	1.425
5c	−7.72 mm	−0.26	3.11 mm	1.000
6b	$\infty$	0.00	$\infty$	1.000
6c	11.65 mm	−9.24	13.00 mm	1.523
7	−9.48 mm	−1.07	$\infty$	1.000

infinite working distance. Such an imaging system will also have a large depth of field, and, thus, extracting depth information from focus will be insensitive to object position.

### B. Vitrectomy Lenses

Plano-concave lenses allow for the visualization of devices operating in the vitreous humor of phakic (i.e., intact intraocular lens) eyes [22]. In Fig. 2(b), the vitrectomy lens S5.7010 from HUCO Vision SA [11] is shown. Its optical parameters can be found in Table I. Vitrectomy lenses increase the field of view (up to  $40^\circ$ ), attenuate the virtual images formed by the eye optics, and position them inside the eye. The virtual images are subsequently captured by an additional imaging system. Larger lenses capture more rays that escape the pupil by limiting vignetting and increasing the field of view. Vitrectomy lenses result in virtual images that span a shorter distance than in direct ophthalmoscopy, allowing the imaging system to have a shorter working distance (see Fig. 3 dashed line) and depth of field. However, the working distance must be at least 20 mm to image the retina, and since depth of field is proportional to it, there is a fundamental limit to the depth-from-focus resolution achievable with vitrectomy lenses.

### C. Indirect Ophthalmoscopy

Indirect ophthalmoscopy uses condensing lenses that create an aerial image of the surface of the retina. Contrary to other ophthalmoscopy methods, indirect ophthalmoscopy allows a wide field of view (even up to  $100^\circ$ ) to be observed. The field of view is governed not only by the refractive index and the shape of the condensing lens surfaces but also by the diameter of the lens itself and its position with respect to the cornea. Due to

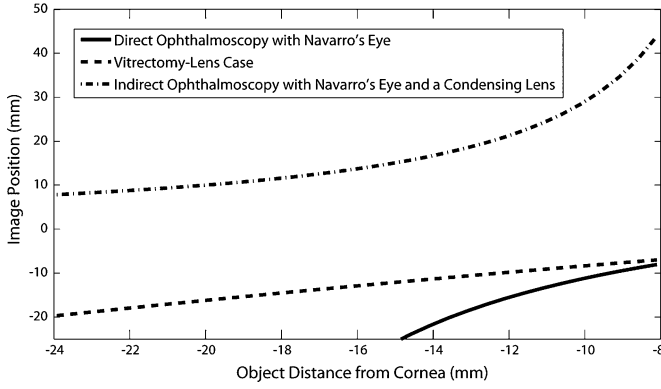


Fig. 3. Image position versus intraocular object position for the systems in Fig. 2. Image distances are measured from the final surface of each optical system (5a, 6b, 7, respectively).

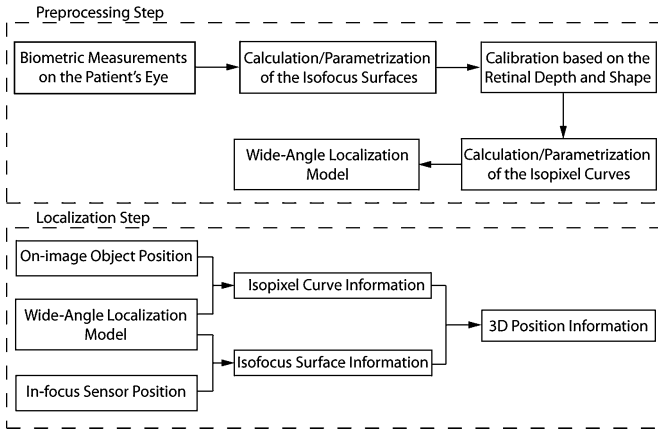


Fig. 4. Flowchart for the proposed wide-angle localization algorithm.

vignetting, there are always some rays that escape the eye and are not captured by the lens, thus, limiting the maximum achievable field of view. State-of-the-art condensing lenses and their design considerations are discussed in [12]. From simulations of a system composed of Navarro's schematic eye equipped with a condensing lens (see Fig. 2(c) and Table I), the aerial image position versus the on-axis object position can be estimated (see Fig. 3 dashed-dotted line). The results indicate that if the aerial image is directly captured by an imaging system with a shallow depth of field, both a high field of view and accurate focus-based localization can be achieved. Because of these reasons, indirect ophthalmoscopy is the most appropriate method for focus-based localization.

### III. WIDE-ANGLE INTRAOCULAR LOCALIZATION

In [19], an algorithm for intraocular localization based on paraxial approximations was presented. However, in order to take advantage of the full field of view that indirect ophthalmoscopy offers, one must go beyond the simple paraxial models. We propose a method that is based on raytracing on an optical model of the human eye that can be constructed pre-operatively. Methods to extract individual eye parameters are described in [24] and [25]. Recently, a method that creates per-

TABLE II  
OPTICAL PARAMETERS FOR THE CONDENSING LENS OF SECTION III

Surface	Posterior	Anterior
Radius of Curvature (mm)	11.65	-9.48
Conic Constant	-9.24	-1.07
$a_4$	$4.078 \times 10^{-5}$	0.0
$a_6$	$-1.542 \times 10^{-7}$	0.0
$a_8$	$-2.647 \times 10^{-9}$	0.0
$a_{10}$	$2.023 \times 10^{-11}$	0.0
Thickness (mm)	13.00	$\infty$
Refractive Index	1.523	1.000

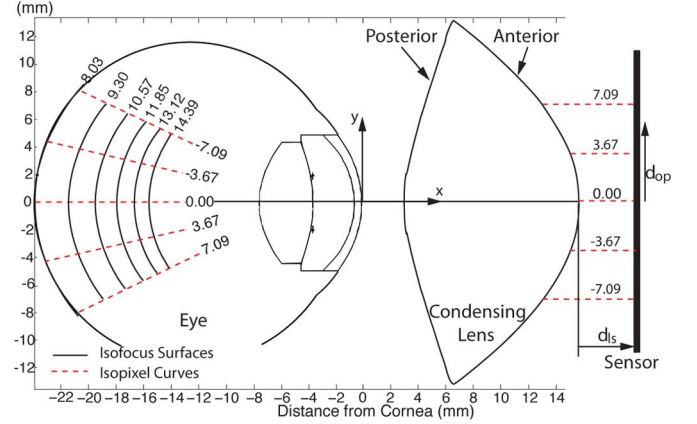


Fig. 5. Simulation of the isofocus surfaces and isopixel curves for the system of Fig. 2(c). The different isofocus surfaces correspond to the distance from the lens to the sensor ( $d_{is}$ ), for uniform sensor steps of  $\sim 1.27$  mm. The isopixel curves correspond to pixel distances from the optical axis ( $d_{op}$ ).

sonalized eye models from biometric measurements was proposed [26].

Our proposed algorithm can be applied to any type of imaging system that has a shallow depth of field. A flowchart of the algorithm can be seen in Fig. 4. The analysis that follows considers a simple imaging system consisting of a condensing lens that creates a flat, aerial retinal image and an image sensor that captures this image. The condensing lens is composed of one aspheric surface and one pure conic surface (see Table II and Fig. 5). The aspheric components were estimated through an iterative procedure that reduced the image's field curvature, for a field of view of  $60^\circ$ – $70^\circ$ . Since Navarro's eye is valid for a field of view up to  $70^\circ$ , it is not necessary to optimize the condensing lens for a greater field of view. The initial lens' parameters were taken from [12], based on the requirement for a flat aerial retinal image with a high field of view. The surfaces of the condensing lens are given by

$$x = \frac{y^2/R}{1 + \sqrt{1 - ((c+1)y^2)/(R^2)}} + a_4 y^4 + a_6 y^6 + a_8 y^8 + a_{10} y^{10} \quad (1)$$

where  $R$  is the radius of curvature,  $c$  is the conic constant,  $x$  is measured on the optical axis,  $y$  is the distance from the optical axis, and  $a_4$ ,  $a_6$ ,  $a_8$ , and  $a_{10}$  are the aspheric coefficients. Initially, we determined  $a_4$  by reducing the image's field of curvature as much as possible, and we proceeded sequentially determining  $a_6$ ,  $a_8$ , and  $a_{10}$  to reduce it further. A similar iterative optimization method for condensing lenses is described in [27].

Since our method relies on focus information, we calculate the depth of focus for this particular lens design. Using paraxial equations [28, p. 404], we have

$$\delta = \frac{n_v}{A_N} (1 + m) c \quad (2)$$

where  $\delta$  is the depth of focus,  $m = 0.76$  is the system's magnification,  $n_v = 1.336$  is the refractive index of the vitreous humor,  $A_N = 0.159$  is the numerical aperture, and  $c$  is diameter of the circle of confusion. For the case, where the image is captured directly by an image sensor with a  $6.4 \mu\text{m} \times 6.4 \mu\text{m}$  sensing element,  $c = 6.4 \mu\text{m}$ . The depth of focus is then estimated at  $\delta = 95 \mu\text{m}$ . Finally, using the slope in Fig. 3 (dashed-dotted line), we can estimate the depth of field at approximately  $150 \mu\text{m}$ ; this is the theoretical resolution of our algorithm.

As stated previously, the condensing lens projects the surface of the retina on a flat aerial image. One expects that moving the sensor will focus the image at different surfaces inside the eye; we call these surfaces *isofocus* surfaces. Moreover, locations inside the eye will correspond to pixels on a moving sensor in a way that differs from the perspective projection model; we call the locus of intraocular points that is imaged on the same pixel coordinates an *isopixel* curve. The locations of the isofocus surfaces and isopixel curves are dependent on the condensing lens and the individual eye.

We estimate the isofocus surfaces and the isopixel curves by ray tracing. Due to the rotational symmetry of the system, we examine the 2-D case. For a grid of points inside Navarro's eye, a fan of rays is traced to the sensor position. We position the sensor plane so that the spot size created by this rayfan is minimized (i.e., the image is in focus). The 2-D coordinates on the sensor plane where the rayfan is focused specify the pixel coordinates on the image. With the calculated information, we create the isofocus surfaces and isopixel curves. In theory, there is an infinite number of isofocus surfaces and isopixel curves, but in practice only a limited number needs to be estimated due to the resolution of sensor movement and pixel size, respectively. We estimate the resolution of isofocus surfaces based on our previous paraxial depth of field estimated at  $150 \mu\text{m}$ . Results for the area of validity of the Navarro's eye can be seen in Fig. 5. The position of an intraocular point can be estimated from the intersection of its isopixel curve (determined from its pixel coordinates on the in-focus image) with its isofocus surface (determined from the displacement of the sensor with respect to the condensing lens).

Fig. 5 shows that the expected depth resolution is higher for regions farther from the retina. Moreover, it shows that the formed image is inverted. From the slope of the isopixel curves, it can be seen that the magnification of the intraocular object increases farther from the retina. As a result, we conclude that spatial resolution increases for positions closer to the intraocular lens.

In order to be able to perform intraocular localization unambiguously, the parameters of the isofocus surfaces and isopixel curves should be injective ("one-to-one") functions of the sensor position and the pixel coordinates, respectively.

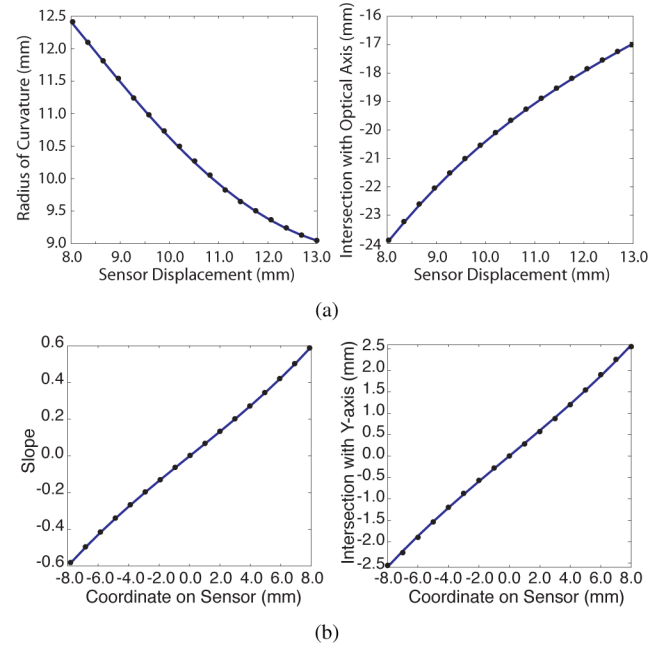


Fig. 6. Parameterization polynomials for the optical system of Fig. 5. (a) Isofocus surface parameterization: fitted third-order polynomials for the radius of curvature and for the intersection with the optical axis, respectively. (b) Isopixel curve parameterization: fitted third-order polynomials for the line slope and for the intersection with the  $y$ -axis, respectively.

#### A. Surface and Curve Parameterization

The isofocus surfaces result from the optics of a rotationally symmetric and aligned system composed of conic surfaces. Therefore, it is assumed that they are also conic surfaces that can be parameterized by their conic constant, radius of curvature, and intersection with the optical axis. Since the isofocus surfaces correspond to a specific sensor position, their three parameters can also be expressed as functions of the sensor position. The radius of curvature and intersection with the optical axis parameters of the fitted surfaces are displayed in Fig. 6(a) as polynomial functions of the sensor position. For each parameter, we fit the least-order polynomial that captures its variability effectively. Navarro's eye has a retinal surface of zero conic constant (i.e., its retina is spherical), therefore, the conic constant of the isofocus surfaces is set to zero. Our simulations show that the variation of the isofocus surfaces can be captured successfully by changes in the curvature.

The isopixel curves are lines, and it is straightforward to parameterize them using their slope and their intersection with the  $y$ -axis, given a coordinate frame. Each isopixel curve corresponds to one pixel on the image, and its parameters are functions of the pixel's offset (measured from the image center) due to the rotational symmetry of the system. For the 2-D case, two parameters are required. The parameters of the fitted lines are shown in Fig. 6(b) as polynomial functions of the pixel's coordinate on the image sensor. For each parameter, we fit the least-order polynomial that captured its variability effectively.

As can be seen in Fig. 6, the parameterizing functions are indeed injections. As a result, intraocular localization can be



unambiguous, and 3-D wide-angle intraocular localization with this technique is possible.

### B. Sensitivity Analysis

Estimating the accuracy in the measurement of different eye parameters involves synthesizing information from measurements acquired *ex vivo* and *in vivo*. This results in large errors, and as a result, the results reported on this topic are limited. Moreover, the repeatability and reproducibility of the optical measurements is an ongoing debate among clinicians, and different groups occasionally report conflicting results [29]. Thus, in order to evaluate the potential of the proposed wide-angle intraocular localization algorithm, we must estimate its behavior with respect to inaccuracies in the modeling.

To achieve this, we first modify the eye model by individually perturbing each of the optical elements of the Navarro's model. Next, we raytrace from intraocular points that cover  $70^\circ$  of the eye's field of view until the image. Finally, we use the position where the image is formed (the in-focus sensor position), and the position of the projections on the image (pixel coordinates) to estimate the 3-D position of the original intraocular points. In this case, however, we use the isopixel surfaces and isopixel curves estimated for the unperturbed Navarro's model. As a result, there are errors in the estimated positions. These errors enable us to understand how uncertainties in the different optical parameters affect the localization results and, therefore, which optical elements mostly affect intraocular localization.

Since Navarro's model is based on anatomical data, for the perturbations in the eye parameters we apply the standard deviations reported in the literature. For each optical element, we span its parameter space and calculate the maximum localization error. A similar analysis to estimate the effect of parameter changes in the optic power of the eye and the intraocular lens is conducted in [30] and [31], respectively. However, [30] uses thin-lens equations, which are not appropriate for the wide-angle case, and [31] uses the standard deviation of the mean instead of the standard deviation of the population, and consequently underestimates uncertainties.

The first optical element that rays emanating from intraocular objects pass through is the vitreous humor. The vitreous humor of the human eye is a viscoelastic fluid that is composed of 99% water. The refraction index of water is 1.333, and the refractive index of the vitreous humor in Navarro's model is 1.336. We assume a variation of  $\pm 2\%$  in this parameter. The maximum localization errors that result by assuming such an uncertainty can be seen in Fig. 7(a).

The intraocular lens is a gradient refractive index lens, and its precise characterization is an open research topic [32], [33]. This is why schematic eye models typically propose an equivalent intraocular lens with a constant refractive index of 1.42 [10], [30], though there is ongoing work to consider its special refractive index distribution [34], [35]. Based on this, it is difficult to establish uncertainty margins for this parameter, so we examine a large variation of constant refractive indexes (1.363–1.476). In [25], the anterior and posterior radii of curvature of the intraocular lens were measured using an autokeratometer, and the

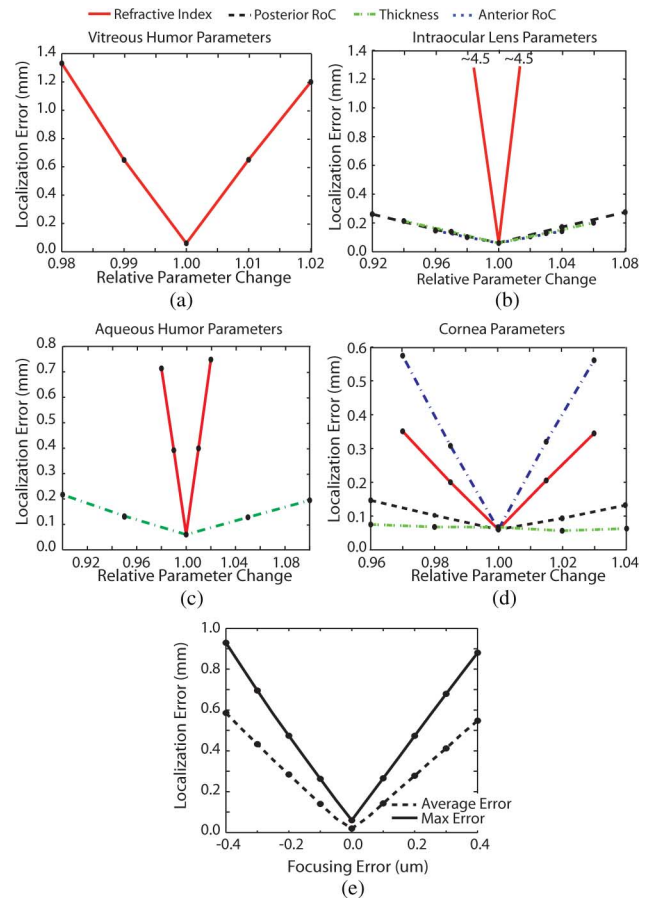


Fig. 7. Maximum localization errors due to parameter uncertainty. (a) Vitreous humor. (b) Intraocular lens. (c) Aqueous humor. (d) Cornea. (e) Focusing. RoC: Radius of Curvature.

extracted variations were  $\pm 4\%$  and  $\pm 8\%$ , respectively (9 patients). In [36], the lens thickness was measured for 30 adult emmetropic eyes and the resulting variation was  $\pm 6\%$ , whereas in [25], the variation was calculated at  $\pm 3\%$ . The maximum localization errors that these uncertainties lead to are displayed in Fig. 7(b). This figure shows that the greatest errors are caused by uncertainties in the refractive index of the intraocular lens. Maximum uncertainty in this parameter leads to errors of approximately 4.5 mm.

Similarly to the vitreous humor, the aqueous humor consists primarily of water. We assume the same variation in its refractive index ( $\pm 2\%$ ). The thickness of the anterior chamber was measured in [36], and the variation between 113 patients was  $\pm 10\%$ . In [25], the variation was estimated at  $\pm 6\%$ . The maximum resulting localization errors can be seen in Fig. 7(c).

Methods to measure the cornea of the human eye are reported in [37] and [38]. Both efforts report variations of  $\pm 3\%$  for the corneal anterior radius of curvature after measuring 100 and 114 patients, respectively. The variations of the corneal thickness and the posterior radius of curvature are calculated as  $\pm 6\%$  and  $\pm 4\%$ , respectively. The refractive index of the cornea was measured for 10 eyes in [39]. The conclusion is that the anatomical elements of the cornea (epithelium, anterior surface, posterior surface) have different refractive indexes, and

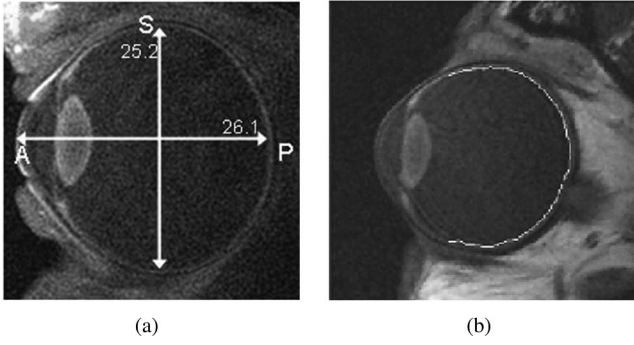


Fig. 8. Biometric measurements from MRI images. (a) Axial length. (b) Retinal shape. (Reprinted with permission from ARVO.)

their values range from 1.372 to 1.406. Given that the mean corneal refractive index from [10] is 1.376, we conclude that the variation in the refractive index is 3%. In Fig. 7(d) we show the maximum errors resulting from each uncertainty. The most sensitive parameter is the anterior radius of curvature.

The condensing lens can be machined with micrometer accuracy (errors less than 0.1% based on personal communication with Sumipro bv. [40]), and its refractive index is that of well-known materials. We can thus assume that there is no variation in its parameters.

In Fig. 7(e), we show the mean and maximum localization errors attributed to the miscalculation of focus. Better focus estimation is achieved by selecting the appropriate focus-scoring algorithm from [41].

Based on Fig. 7, there are a number of parameters that, if misestimated, can lead to high localization errors. The five most important eye parameters are: 1) refractive index of the intraocular lens; 2) refractive index of the vitreous humor; 3) anterior radius of curvature of the cornea; 4) refractive index of the aqueous humor; and 5) refractive index of the cornea. This sensitivity analysis and our discussion point to the fact that for the localization algorithm to be successful, calibration procedures that can handle the uncertainties in different parameters are needed.

### C. Calibration

Preliminary experiments show that calibration of the isopixel curves is not necessary, because their relative impact on the localization accuracy is low. It is the intersection of the isofocus surfaces with the optical axis (see Fig. 6(a) right) that has the greatest effect on localization.

Ideally, one would perform an on-optical-axis depth-from-focus experiment, and calibrate for the relationship between the in-focus sensor position and the depth of the object by using the full set of data points. However, such an approach would be invasive, and would require a vitrectomy. The depth and shape of the retina though can be noninvasively extracted from MRI data [42], [43] (see Fig. 8).

The proposed calibration method uses a first-order model of the optics of the system. First-order optics accurately describe the image formation of on-axis objects. We assume that the optical modeling has accumulated errors that can be lumped

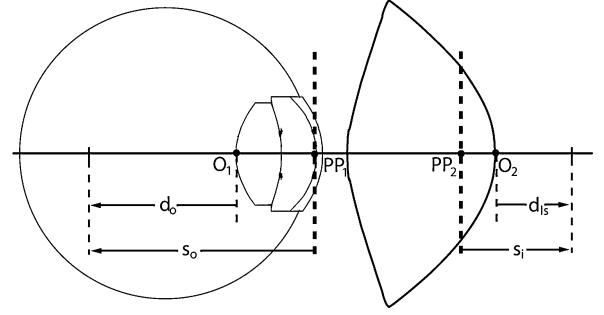


Fig. 9. Illustration of the first-order optical model for the system of Navarro's eye with a condensing lens. PP: Principal point.

and included as errors in the estimated image and object positions. We can afterwards calibrate the imaging system using only the retinal depth of a patient's eye. The analysis that follows demonstrates that this method suppresses the errors caused by large uncertainties in the eye's optical parameters.

We extract the first-order optical model of Navarro's eye with the condensing lens (see Fig. 9) by calculating the principle points/planes using OSLO. We verified that OSLO performs the paraxial calculations as described in [44] and [45]. In this framework, each lens is described by three matrices (two refraction matrices  $\mathcal{R}_1$  and  $\mathcal{R}_2$ , and one transfer matrix  $\mathcal{T}_{21}$ )

$$\mathcal{R}_1 = \begin{bmatrix} 1 & -\mathcal{D}_1 \\ 0 & 1 \end{bmatrix}, \quad \text{where } \mathcal{D}_1 = \frac{n_l - n_o}{r_1} \quad (3)$$

$$\mathcal{R}_2 = \begin{bmatrix} 1 & -\mathcal{D}_2 \\ 0 & 1 \end{bmatrix}, \quad \text{where } \mathcal{D}_2 = \frac{n_i - n_l}{r_2} \quad (4)$$

$$\mathcal{T}_{21} = \begin{bmatrix} 1 & 0 \\ t/n_l & 1 \end{bmatrix} \quad (5)$$

where the subscripts 1 and 2 refer to the posterior and anterior surfaces of the lens, respectively,  $n_l$  is the refractive index of the lens,  $n_o$  is the refractive index of the environment on the object side,  $n_i$  is the refractive index of the environment on the image side,  $r_1$  and  $r_2$  are the radii of curvature, and  $t$  is the thickness of the lens. Then, the focal length and the principal points of the lens can be found by

$$\mathcal{A} = \begin{bmatrix} a_{11} & a_{12} \\ a_{21} & a_{22} \end{bmatrix} = \mathcal{R}_2 \mathcal{T}_{21} \mathcal{R}_1 \quad (6)$$

$$f = -\frac{1}{a_{12}} \quad (7)$$

$$[O_1, PP_1] = \frac{n_o(1 - a_{11})}{-a_{12}} \quad (8)$$

$$[O_2, PP_2] = \frac{n_i(a_{22} - 1)}{-a_{12}} \quad (9)$$

where  $f$  is the effective focal length, and the operator  $[\cdot, \cdot]$  is the signed distance between two points. For Navarro's eye equipped with a condensing lens, the matrices corresponding to all the lenses are multiplied

$$\mathcal{A} = \mathcal{R}_{cl2} \mathcal{T}_{cl21} \mathcal{R}_{cl1} \mathcal{T}_{air} \mathcal{R}_{co2} \mathcal{T}_{co21} \mathcal{R}_{co1} \mathcal{T}_{aq} \mathcal{R}_{il2} \mathcal{T}_{il21} \mathcal{R}_{il1} \quad (10)$$

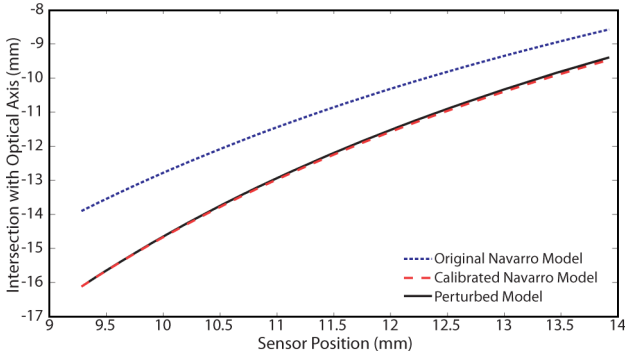


Fig. 10. Effects of biometric calibration on a system with 3% uncertainty in the refractive index of the intraocular lens. We assume the retinal depth is known precisely.

where  $\{\mathcal{R}, \mathcal{T}\}_{cl}$  are the matrices that correspond to the condensing lens,  $\{\mathcal{R}, \mathcal{T}\}_{co}$  are the matrices that correspond to the cornea,  $\{\mathcal{R}, \mathcal{T}\}_{il}$  are the matrices that correspond to the intraocular lens,  $\mathcal{T}_{air}$  is the matrix corresponding to the air between the condensing lens and the cornea, and  $\mathcal{T}_{aq}$  is the matrix corresponding to the aqueous humor between the cornea and the intraocular lens. Then, the effective focal length and the principal points/planes for Navarro's eye equipped with the condensing lens can be calculated from (6)–(9).

The compound optical system projects an object at  $s_o$  to an image on the sensor at  $s_i$

$$s_i = d_{ls} + [O_2, PP_2] + e_{d_{ls}} \quad (11)$$

$$s_o = -\frac{f n_v s_i}{s_i - f} \quad (12)$$

$$d_o = s_o - [O_1, PP_1] + e_{d_o} \quad (13)$$

where  $n_v$  is the refractive index of the vitreous humor,  $d_{ls}$  is the distance from the condensing lens where the image is formed, and  $e_{d_o}$  and  $e_{d_{ls}}$  are the lumped errors in the estimated object and image positions, respectively.

In (11)–(13), the parameters are calculated using paraxial approximation formulas. However, due to the inclusion of the conic and aspheric components in the condensing lens (see Table II), these parameters need to be refined. We use the paraxial calculations as a starting point, and perform a minimization so that (11)–(13) accurately describe the behavior of the intersection of the isofocus surfaces with the optical axis.

Using (11)–(13) and only the measured retinal depth and its corresponding in-focus sensor position, we estimate the  $e_{d_{ls}}$  and  $e_{d_o}$  that minimize the error in the estimated retinal intraocular depth. Assuming perfect knowledge of the retinal depth, the calibration results for 3% uncertainty in the refractive index of the intraocular lens can be seen in Fig. 10.

In [42], after measuring the ocular axial length of 22 adult emmetropes and 66 adult myopes with magnetic resonance imaging (MRI) scans, errors up to 0.3 mm between measurements of the same patient of any category were reported. Comparison of the MRI-based results with A-scan ultrasonography reported good agreement across patients ( $0.3 \pm 0.2$  mm). We take these inaccuracies into account, and calculate the resulting maximum

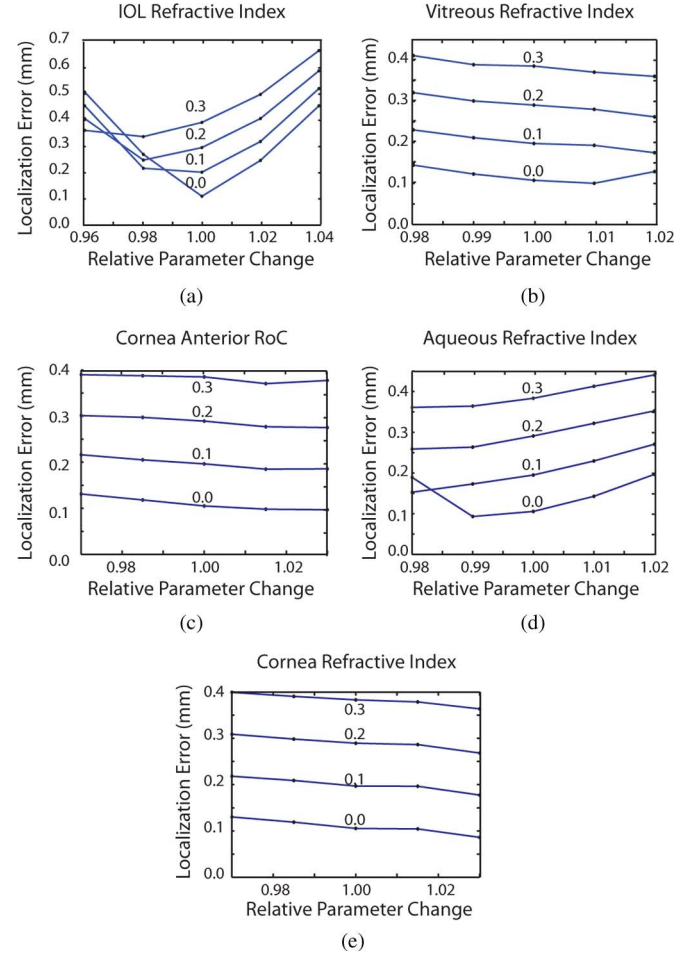


Fig. 11. Localization error due to parameter uncertainty after calibration for the five most crucial parameters of Fig. 7. (a) Intraocular lens refractive index. (b) Vitreous humor refractive index. (c) Cornea anterior radius of curvature. (d) Aqueous humor refractive index. (e) Cornea refractive index. The errors (in mm) in the retinal depth estimation are shown above each curve.

wide-angle localization error for the variations in the optical eye parameters to which localization is most sensitive. The results can be seen in Fig. 11. Comparison with Fig. 7 shows that this calibration procedure indeed suppresses the localization errors, and accurate retinal depth measurements greatly reduce them. Maximum uncertainty in the retinal depth will lead to final maximum localization errors not larger than 400  $\mu$ m for most parameters.

#### IV. LOCALIZATION IN A MODEL EYE

To demonstrate the proposed wide-angle localization method, we use an appropriate imaging system and perform wide-angle focus-based localization in a model eye.

##### A. Experimental Setup

As an experimental testbed, we use the model eye [9] from Gwb International, Ltd. This eye is equipped with a plano-convex lens that mimics the compound optical system of the human eye. The model eye contains no liquid, and thus, the lens

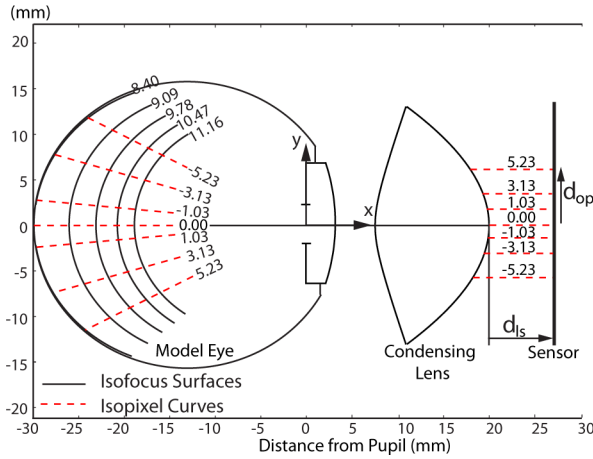


Fig. 12. Simulation of the isofocus surfaces and isopixel curves for the system composed of the model eye and the condensing lens. The different isofocus surfaces correspond to the distance from the lens to the sensor ( $d_{is}$ ), for uniform sensor steps of  $\sim 0.7$  mm. The isopixel curves correspond to pixel distances from the optical axis ( $d_{op}$ ).

can be used by itself. Gwb International, Ltd. disclosed the lens' parameters so that simulations can be performed accurately. The dimensions of the model eye were measured to estimate its retinal depth and shape.

The imaging device consists of two components: a condensing lens that is kept at a constant position with respect to the eye and a sensor that captures the aerial image directly and moves with respect to the lens to focus on objects throughout the eye. The condensing lens is a custom-made double conic-convex lens based on [12] (see Fig. 2(c) for parameters, where the refractive index was changed to 1.531 due to lack of the original material at Sumipro bv.). This lens causes a  $0.78\times$  magnification, thus, an object of  $100\ \mu\text{m}$  near the retina would create an image of  $78\ \mu\text{m}$ . The image is captured by a firewire Basler A602f camera with a CMOS sensor ( $9.9\ \mu\text{m} \times 9.9\ \mu\text{m}$  sensing element,  $640 \times 480$  noninterpolated resolution). The camera and the object were moved using two M-285 Sutter linear micromanipulation stages. The focus score was calculated using the normalized variance of the captured image. According to [41], the normalized variance is the most robust image focusing metric for noisy images.

### B. Isofocus Surfaces and Isopixel Curves

The simulated isofocus surfaces and isopixel curves of the composite system are shown in Fig. 12. Their parameterization is shown in Fig. 13. The behavior of the parameters is similar to the one displayed in Fig. 6. The assumed conic constant of the isofocus surfaces is kept constant at  $-0.175$ , which is the value we measured for the retina of the model eye.

### C. Depth of Focus and Resolution

Using (2), we calculate the depth of focus for this optical system at  $83\ \mu\text{m}$ . The circle of confusion is given from the Basler A602f sensing element, and the remaining parameters can be calculated through OSLO. This is an estimation of the variance

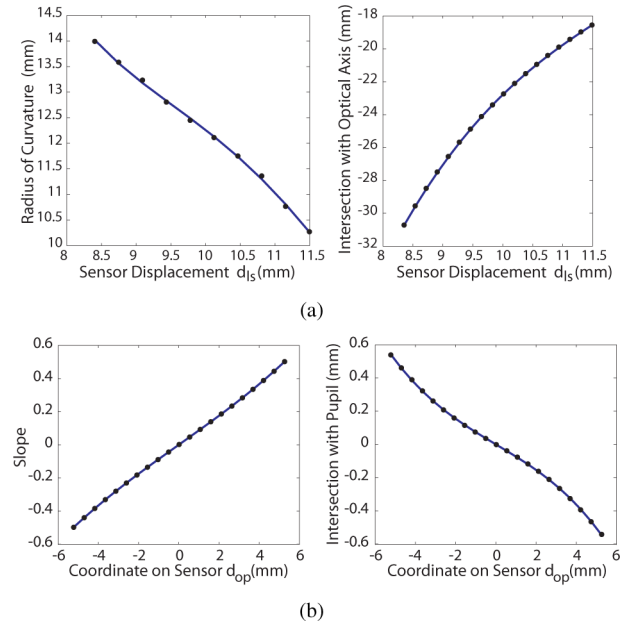


Fig. 13. (a) Isofocus surface parameterization: fitted third-order polynomials for the curvature and for the intersection with the optical axis. (b) Isopixel curve parameterization: fitted third-order polynomials for the slope and for the intersection with the pupil.

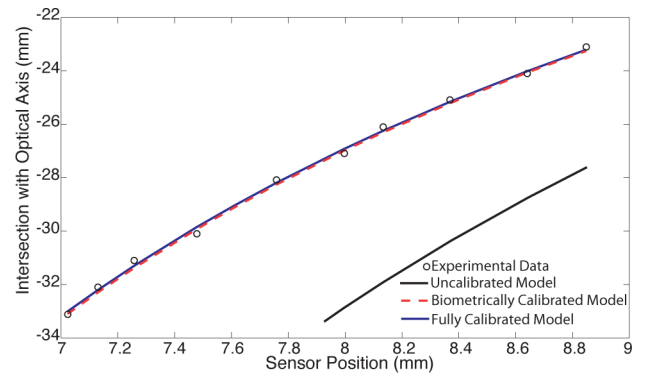


Fig. 14. Different model fits for the function describing the intersection of isofocus surfaces with the optical axis (measured from the pupil) with respect to the in-focus sensor position.

in the in-focus sensor position. From the slope of Fig. 13(a) (right), we can calculate depth of focus, which is the expected resolution of the isofocus surfaces, at  $500\ \mu\text{m}$ .

### D. Calibration

In order to calibrate the isofocus surfaces for their intersection with the optical axis, we perform an on-optical-axis depth-from-focus experiment on the aligned optical system. The estimated in-focus sensor positions with respect to different depths in the model eye can be seen in Fig. 14. We calibrate using the method of Section III-C. The parameters required for (11)–(13) were measured 30 times for accuracy (retinal depth  $33.1 \pm 0.55$  mm, interlens distance  $d_{is} = 3.59 \pm 0.18$  mm). Fig. 14 shows the calibration results. The fully calibrated model corresponds to the fit that is generated when all the points from the on-optical-axis depth-from-focus experiment are used. In a clinical setting, such



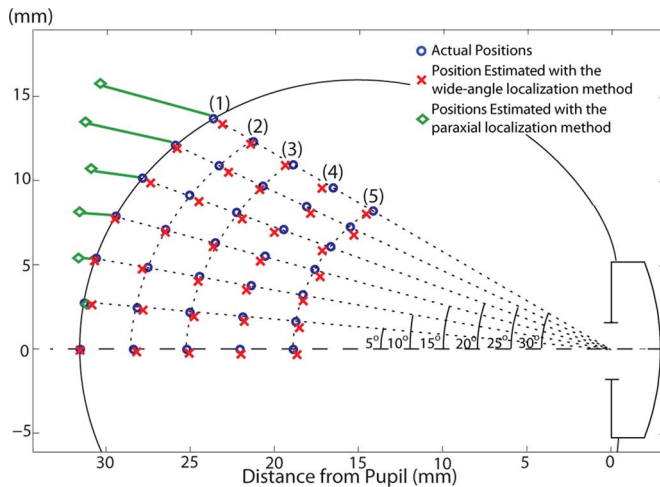


Fig. 15. Localization experiment showing the validity of the wide-angle localization algorithm. Experiment is shown for the condensing lens [12], and the model eye [9]. The paraxial model of [19], which loses accuracy away from the optical axis, is also shown for comparison.

knowledge would be unavailable. The biometrically calibrated object corresponds to the fit that is generated when only the retinal depth is used. As can be seen, the biometric calibration adjusts the model to correspond to the experimental observations. The uncalibrated model from Fig. 13(a) (right) is shown for comparison.

The remaining two parameters of the isofocus surfaces control the shape of the isofocus surfaces, but not their position. Our experiments have shown that we can in fact capture an overall sharp image of the entire model eye's retina using the condensing lens. Therefore, we conclude that there exists an isofocus surface that corresponds to the retinal surface, and we consider it as the first surface. From Fig. 12, we see that the first isofocus surface does indeed roughly correspond to the retinal shape. As a result, calibration for the conic constant and the curvature is not needed. If the model did not accurately predict the shape of the retina, yet an in-focus image of the retina was obtained, then we would also calibrate the parameters of the first isofocus surface so that it has the same shape as the retina. It is not guaranteed that an isofocus surface corresponds to the entire retina for every eye (i.e., the possibility of an in-focus image of the entire retina is not guaranteed), however, this is also not a requirement for the localization algorithm.

### E. Results

In order to validate the wide-angle localization algorithm, we performed a localization experiment for various angles with respect to the optical axis and various distances from the pupil. We repeated the experiment 30 times for each point and calculated the mean and variance in the in-focus sensor position. The calculated variances for the parameters of the algorithm allow the calculation of the uncertainty of the estimations [46].

Fig. 15 displays the results of the proposed wide-angle localization algorithm. For comparison, we show the results based on the paraxial localization algorithm presented in [19] for the

TABLE III  
ERRORS (UNCERTAINTY IN  $\mu\text{m}$ ) FOR THE EXPERIMENT IN FIG. 15

	surfaces				
	1	2	3	4	5
0°	5(102)	201(79)	195(102)	201(119)	271(119)
5°	410(60)	310(52)	285(48)	204(50)	329(85)
10°	125(79)	362(48)	250(60)	331(100)	300(47)
15°	105(156)	100(98)	195(79)	364(55)	394(145)
20°	481(100)	556(73)	381(111)	569(90)	520(364)
25°	126(128)	572(156)	207(55)	393(161)	430(139)
30°	556(153)	162(188)	424(301)	644(186)	405(195)

points on the retina. The predictions of the new localization algorithm remain close to the actual values, but, as expected, the results of paraxial localization deteriorate as the angles increase. The paraxial approximations are colinear since first-order models assume a plane-to-plane image formation, whereas the condensing lens creates a flat image of the retina.

In Table III, the experimentally measured localization errors with respect to increasing angles and distances from the pupil are shown. The rows show the errors for varying distances from the pupil and the columns show the errors for varying angles. The errors are calculated using the mean in-focus sensor position. The number in brackets is the estimated uncertainty in  $\mu\text{m}$  based on the variance in the model parameters and the variance in the in-focus sensor position. The mean error is  $325 \mu\text{m}$ , and the standard deviation is  $158 \mu\text{m}$ . Given that the depth of field of the experimental optical system is  $500 \mu\text{m}$ , our errors are within the theoretical limits of the resolution.

### V. CONCLUSION

We have developed an algorithm that will provide 3-D position information for the partial automation of intraocular surgeries. We examined the common methods of ophthalmoscopy with respect to their imaging and localizing capabilities. We concluded that indirect ophthalmoscopy using an imaging system with a small depth of field is a promising way for wide-angle intraocular imaging and localization. We presented the first wide-angle intraocular localization algorithm using an optical system that is based on state-of-the-art condensing lenses that create a flat retinal aerial image. Our sensitivity analysis identified the parameters of the human eye that are most crucial to localization, and the subsequent proposed calibration method demonstrated the ability to suppress errors that result from misestimated eye parameters. We conducted a wide-angle localization experiment in a model of the human eye, and the localization algorithm showed excellent results (mean error  $325 \mu\text{m}$ ). Errors in this scale satisfy the goal of providing precise position information to the open-loop controller of the electromagnetic system in [8]. In addition to the 3-D position information, closed-loop image-based visual servoing techniques and tracking of the microrobot [47] will enable fully autonomous operations. Thus, for the first time, a technique for wide-angle 3-D intraocular localization is available, and fully autonomous retinal surgeries using untethered tools such as microrobots are one step closer to reality.

## ACKNOWLEDGMENT

The authors would like to thank the reviewers for their comments and their contribution to the quality of this work, and Prof. D. A. Atchison from the School of Optometry, Queensland University of Technology, Brisbane, Queensland, Australia, for providing the high-resolution images for Fig. 8.

## REFERENCES

- [1] M. Dewan, P. Marayong, A. M. Okamura, and G. D. Hager, "Vision-based assistance for ophthalmic micro-surgery," in *Proc. Int. Conf. Med. Image Comput. Comput.-Assisted Intervention*, 2004, pp. 49–57.
- [2] B. Mitchell, J. Koo, I. Iordachita, P. Kazanzides, A. Kapoor, J. Handa, G. Hager, and R. Taylor, "Development and application of a new steady-hand manipulator for retinal surgery," in *Proc. IEEE Int. Conf. Robot. Autom.*, 2007, pp. 623–629.
- [3] C. Riviere, W. Ang, and P. Khosla, "Toward active tremor canceling in handheld microsurgical instruments," *IEEE Trans. Robot. Autom.*, vol. 19, no. 5, pp. 793–800, Oct. 2003.
- [4] W. Wei, R. Goldman, H. Fine, S. Chang, and N. Simaan, "Modeling and performance evaluation of hybrid multi-arm robots operating on hollow suspended organs," *IEEE Trans. Robot.*, vol. 25, no. 1, pp. 147–157, Feb. 2009.
- [5] K. B. Yeşin, K. Vollmers, and B. J. Nelson, "Modeling and control of untethered biomicrobots in a fluidic environment using electromagnetic fields," *Int. J. Robot. Res.*, vol. 25, no. 5–6, pp. 527–536, 2006.
- [6] Z. Nagy, O. Ergeneman, J. J. Abbott, M. Hutter, A. M. Hirt, and B. J. Nelson, "Modeling assembled-MEMS microrobots for wireless magnetic control," in *Proc. IEEE Int. Conf. Robot. Autom.*, 2008, pp. 874–879.
- [7] J. J. Abbott, O. Ergeneman, M. P. Kummer, A. M. Hirt, and B. J. Nelson, "Modeling magnetic torque and force for controlled manipulation of soft-magnetic bodies," *IEEE Trans. Robot.*, vol. 23, no. 6, pp. 1247–1252, Dec. 2007.
- [8] M. P. Kummer, J. J. Abbott, B. E. Kratochvil, R. Borer, A. Sengul, and B. J. Nelson, "OctoMag: An electromagnetic system for 5-DOF wireless micromanipulation," in *Proc. IEEE Int. Conf. Robot. Autom.*, 2010, pp. 1610–1616.
- [9] Model eye (3 mm pupil), Gwb International, Ltd., Marshfield Hills, MA, 2010. [Online]. Available: [http://www.gwbinternational.com/model\\_eye.htm](http://www.gwbinternational.com/model_eye.htm)
- [10] I. Escudero-Sanz and R. Navarro, "Off-axis aberrations of a wide angle schematic eye model," *J. Opt. Soc. Amer. A*, vol. 16, no. 8, pp. 1881–1891, 1999.
- [11] S5.7010 lens, FCI Ophthalmics, Pembroke, MA, 2010. [Online]. Available: <http://www.fci-ophthalmics.com/html/retina.html#lenses>
- [12] D. A. Volk, "Indirect ophthalmoscopy lens for use with split lamp or other biomicroscope," U.S. Patent 5 706 073, Jan. 6, 1998.
- [13] T. Drummond and R. Cipolla, "Real-time visual tracking of complex structures," *IEEE Trans. Pattern Anal. Mach. Intell.*, vol. 24, no. 7, pp. 932–946, Jul. 2002.
- [14] J. Ens and P. Lawrence, "An investigation of methods for determining depth from focus," *IEEE Trans. Pattern Anal. Mach. Intell.*, vol. 15, no. 2, pp. 97–108, Feb. 1993.
- [15] M. Subbarao and G. Surya, "Depth from defocus: A spatial domain approach," *Int. J. Comput. Vis.*, vol. 13, no. 3, pp. 271–294, 1994.
- [16] R. Luo, X. Y. Yang, X. F. Peng, and Y. F. Sun, "Three-dimensional tracking of fluorescent particles applied to micro-fluidic measurements," *J. Micromech. Microeng.*, vol. 16, no. 8, pp. 1689–1699, 2006.
- [17] M. Wu, J. W. Roberts, and M. Buckley, "Three-dimensional fluorescent particle tracking at micron-scale using a single camera," *Exp. Fluids*, vol. 38, no. 4, pp. 461–465, 2005.
- [18] K. B. Yeşin, K. Vollmers, and B. J. Nelson, "Guidance of magnetic intraocular microrobots by active defocused tracking," in *Proc. IEEE/RSJ Int. Conf. Intell. Robots Syst.*, 2004, vol. 4, pp. 3309–3314.
- [19] C. Bergeles, K. Shamaei, J. J. Abbott, and B. J. Nelson, "On imaging and localizing untethered intraocular devices with a stationary camera," in *Proc. IEEE Int. Conf. Biomed. Robot. Biomechatron.*, 2008, pp. 489–494.
- [20] C. Bergeles, K. Shamaei, J. J. Abbott, and B. J. Nelson, "Wide angle intraocular imaging and localization," in *Proc. Int. Conf. Med. Image Comput. Comput. Assist. Intervent.*, 2009, pp. 540–548.
- [21] C. Bergeles, K. Shamaei, J. J. Abbott, and B. J. Nelson, "Wide angle localization of intraocular devices from focus," in *Proc. IEEE/RSJ Int. Conf. Intell. Robots Syst.*, 2009, pp. 4523–4528.
- [22] M. P. Snead, M. P. Rubinstein, and P. M. Jacobs, "The optics of fundus examination," *Surv. Ophthalmol.*, vol. 36, no. 6, pp. 439–445, 1992.
- [23] G. Smith and D. A. Atchison, *The Eye and Visual Optical Instruments*. Cambridge, U.K.: Cambridge Univ. Press, 1997.
- [24] Y. Mejia-Barbosa and D. Malacara-Hernandez, "A review of methods for measuring corneal topography," *Optom. Vis. Sci.*, vol. 78, no. 4, pp. 240–253, 2001.
- [25] T. Kirschkamp, M. Dunne, and J. C. Barry, "Phakometric measurement of ocular surface radii of curvature, axial separations and alignment in relaxed and accommodated human eyes," *Ophthalmic Physiol. Opt.*, vol. 24, no. 2, pp. 65–73, 2004.
- [26] R. Navarro, L. Gonzalez, and J. O. S. L. Hernandez-Matamoros, "On the prediction of optical aberrations by personalized eye models," *Optom. Vis. Sci.*, vol. 83, no. 6, pp. 371–381, 2006.
- [27] J. H. Roffman, "Lens design method and resulting aspheric lens," U.S. Patent 5 050 981, Sep. 24, 1991.
- [28] A. Krasznai-Krausz, *The Focal Encyclopedia of Photography*, Fully Revised ed. Burlington, MA: Focal Press, 1965.
- [29] K. Zadnik, D. Mutti, and A. Adams, "The repeatability of measurement of the ocular components," *Invest. Ophthalmol. Vis. Sci.*, vol. 33, no. 7, pp. 2325–2333, 1992.
- [30] D. A. Atchison and G. Smith, *Optics of the Human Eye*. London, U.K.: Butterworth/Heinemann, 2000.
- [31] S. Norrby, "Sources of error in intraocular lens power calculation," *J. Cataract Refract. Surg.*, vol. 34, no. 3, pp. 368–376, 2008.
- [32] M. Campbell, "Measurement of refractive index in an intact crystalline lens," *Vis. Res.*, vol. 24, no. 5, pp. 409–415, 1984.
- [33] C. E. Jones, D. A. Atchison, R. Meder, and J. M. Pope, "Refractive index distribution and optical properties of the isolated human lens measured using magnetic resonance imaging (MRI)," *Vis. Res.*, vol. 45, no. 18, pp. 2352–2366, 2005.
- [34] H. Liou and N. Brennan, "Anatomically accurate, finite model eye for optical modeling," *J. Opt. Soc. Amer. A*, vol. 14, no. 8, pp. 1684–1695, 1997.
- [35] A. V. Goncharov and C. Dainty, "Wide field schematic eye models with gradient-index lens," *J. Opt. Soc. Amer. A*, vol. 24, no. 8, pp. 2157–2174, 2007.
- [36] L. G. Carney, J. C. Mainstone, and B. A. Henderson, "Corneal topography and myopia: A cross-sectional study," *Invest. Ophthalmol. Vis. Sci.*, vol. 38, no. 2, pp. 311–320, 1997.
- [37] S. A. Read, M. J. Collins, L. G. Carney, and R. J. Franklin, "The topography of the central and peripheral cornea," *Invest. Ophthalmol. Vis. Sci.*, vol. 47, no. 4, pp. 1404–1415, 2006.
- [38] M. Dubbelman, V. Sicam, and G. L. Van der Heijde, "The shape of the anterior and posterior surface of the aging human cornea," *Vis. Res.*, vol. 46, no. 6–7, pp. 993–1001, 2006.
- [39] S. Patel, J. Marshall, and F. W. Fitzke, "Refractive index of the human corneal epithelium and stroma," *J. Refractive Surg.*, vol. 11, no. 2, pp. 1100–1105, 1995.
- [40] Sumipro bv, Almelo, The Netherlands, 2010. [Online]. Available: <http://www.sumipro.nl/>
- [41] Y. Sun, S. Duthaler, and B. J. Nelson, "Autofocusing in computer microscopy: selecting the optimal focus algorithm," *J. Microsc. Res. Tech.*, vol. 65, no. 3, pp. 139–149, 2004.
- [42] D. A. Atchison, C. E. Jones, K. L. Schmid, N. Pritchard, J. M. Pope, W. E. Strugnell, and R. A. Riley, "Eye shape in emmetropia and myopia," *Invest. Ophthalmol. Vis. Sci.*, vol. 45, no. 10, pp. 3380–3386, 2004.
- [43] D. A. Atchison, N. Pritchard, K. L. Schmid, D. H. Scott, C. E. Jones, and J. M. Pope, "Shape of the retinal surface in emmetropia and myopia," *Invest. Ophthalmol. Vis. Sci.*, vol. 46, no. 8, pp. 2698–2707, 2005.
- [44] E. Hecht, *Optics*, 4th ed. San Francisco, CA: Addison-Wesley, 2002.
- [45] Lambda Research Corporation, "OSLO optics reference, version 6.1," 2001.
- [46] Joint Committee for Guides in Metrology, *Evaluation of Measurement Data—Guide to the Expression of Uncertainty in Measurement*, 1st ed. JCGM, 2008.
- [47] C. Bergeles, G. Fagogenis, J. J. Abbott, and B. J. Nelson, "Tracking intraocular microdevices based on colorspace evaluation and statistical color/shape information," in *Proc. IEEE Int. Conf. Robot. Autom.*, 2009, pp. 3934–3939.



**Christos Bergeles** (S'04) received the M.S. degree in electrical and computer engineering from the National Technical University, Athens, Greece, in 2006. He is currently working toward the Ph.D. degree at the Institute of Robotics and Intelligent Systems, ETH Zurich, Switzerland, where he is involved in visual tracking and localization of intraocular microrobots.



**Jake J. Abbott** (M'06) received the Ph.D. degree in mechanical engineering from The Johns Hopkins University, Baltimore, MD, in 2005.

During 2005, he was a Postdoctoral Research Associate at the Institute of Robotics and Intelligent Systems, ETH Zurich, Switzerland, and during 2008, he was an Assistant Professor at the University of Utah, Salt Lake City. He is currently the Head of the Telerobotics Laboratory, Department of Mechanical Engineering, University of Utah, where his research involves medical and microscale telerobotics.



**Kamran Shamaei** received the M.S. degree in mechanical engineering from ETH Zurich, Switzerland, in 2009. He is currently working toward the Ph.D. degree at the School of Engineering and Applied Science, Yale University, New Haven, CT, where he is involved in design and development of active orthoses and exoskeletons for patients with spinal cord injuries and pathological gait.



**Bradley J. Nelson** (M'90–SM'06) received the Ph.D. degree in robotics from Carnegie Mellon University, Pittsburgh, PA, in 1995.

He was an Assistant Professor at the University of Illinois, Chicago, during 1995, an Associate Professor at the University of Minnesota, during 1998, and a Professor of robotics and intelligent systems at ETH Zurich, Switzerland, during 2002. He is currently the Head of the Multi-Scale Robotics Laboratory, Institute of Robotics and Intelligent Systems, ETH Zurich, where he is involved in microrobotics and nanorobotics. He is the Chairman of the ETH Electron Microscopy Center.

Dr. Nelson was named to the 2005 "Scientific American 50," and has received multiple Best Conference Paper Awards. His lab won the RoboCup Nanogram competition in 2007 and 2009.